Energy Storage and Conversion 2026, 4(3), 4347.
doi: https://doi.org/10.59400/esc4347

Article

Monte Carlo simulation of a direct beta-radiation harvester: Impact of electric fields

Itzhak Orion[1,*], Adir Cohen[1], Elroei Damri[2]

[1] Department of Nuclear Engineering, Ben-Gurion University of the Negev, Beer-Sheva 8410501, Israel
[2] Nuclear Research Center Negev (NRCN), Beer-Sheva 84190, Israel
*** Corresponding author:** Itzhak Orion, iorion@bgu.ac.il

CITATION

Orion I, Cohen A, Damri E. Monte Carlo simulation of a direct beta-radiation harvester: Impact of electric fields. Energy Storage and Conversion. 2026; 4(3): 4347. https://doi.org/10.59400/esc4347

ARTICLE INFO

Received: 30 April 2026
Revised: 15 June 2026
Accepted: 23 June 2026
Available online: 14 July 2026

Abstract: The viability of high-efficiency direct energy harvesting from a beta-emitting radioactive source was previously experimentally investigated using an apparatus based on an ionization chamber equipped with an internal positioning stage for the source. This novel concept uniquely leverages the direct collection of beta particles on a converter electrode, converting their kinetic energy into electrical power and enabling compact power sources. This approach offers ultra-long-life, maintenance-free solutions in applications where conventional batteries are impractical. To evaluate system performance, we employed Monte Carlo simulations to model electron transport, governed by continuous slowing down due to Coulomb interactions. Electron interactions in matter, dominated by elastic and inelastic scattering, can lead to ionization events accompanied by X-ray fluorescence or Auger electron emission. EGS5 Monte Carlo simulations were performed to study the response of an ionization chamber to a Ni-63 beta source under various electric field strengths. The simulated dosimetric response was compared with previous experimental measurements. Gas-filled ionization chambers, consisting of two electrodes in a controlled electric field, are widely used for radiation dosimetry. Simulations using four different chamber gases across a wide range of field strengths showed consistent agreement with measured dose responses. These results demonstrate that the developed simulation framework is an accurate and versatile tool for investigating electron behavior in gas-filled detectors. It can be confidently applied in future studies to explore alternative gases, field configurations, or radiation sources. Additionally, the findings support the feasibility of direct beta radiation harvesting, highlighting its potential for developing compact and efficient power sources.

Keywords: energy harvesting; beta-radiation; ion-chamber; Monte Carlo; simulation

1. Introduction

1.1. Beta-radiation harvester

The growing demand for sustainable, long-lasting, and compact energy sources has led to renewed interest in nuclear-based power generation at the micro- and nanoscales. A particularly promising direction lies in the use of radionuclides, materials with unstable atomic nuclei that spontaneously emit high-energy particles as they transition toward more stable states. These emissions, which occur independently of environmental conditions such as temperature or pressure, provide a robust and durable energy source. Moreover, certain radionuclides exhibit extremely high energy densities and long half-lives, making them suitable for long-term applications in remote or harsh

environments [1–3].

The utility of radionuclides as power sources, however, depends heavily on the method by which the emitted radiation is converted into usable electrical energy [4–6]. Efficient energy conversion is essential not only for maximizing output but also for ensuring the safe deployment of nuclear energy harvesting systems [7,8]. Radionuclides are typically classified by the type of radiation they emit, such as alpha, beta, or gamma radiation. Alpha and beta emitters are particularly suitable for energy harvesting because their particles can be effectively shielded with simple materials.

Energy harvesting from radionuclides can be broadly divided into thermal and non-thermal techniques. Thermal methods typically involve two conversion stages. First, the kinetic energy of emitted particles is transferred to a material, heating it. Second, this thermal energy is converted into electrical energy using thermionic or thermoelectric devices. Thermionic converters rely on high-temperature electrodes that induce electron flow between a heated emitter and a cooler collector. Although this method is conceptually straightforward, it faces challenges in terms of efficiency and reliability. Thermoelectric conversion, based on the Seebeck effect, generates an electrical voltage across a material subjected to a temperature gradient. Despite being solid-state and thus highly reliable, thermoelectric generators currently achieve efficiencies of only about 7% [9], constrained by material performance, heat losses, and Carnot efficiency limits. Furthermore, in small-scale devices, the temperature gradients are often insufficient to sustain meaningful energy conversion.

To address the limitations of thermal methods, non-thermal direct energy conversion techniques have gained attention. One such technique is the direct-charging beta radiation battery, which uses the kinetic energy of beta particles to generate electric potential directly, without any intermediate thermal stages. This technique can be implemented using three basic configurations [10]: (1) a primary current collector with vacuum insulation, (2) a primary collector with solid dielectric, and (3) a secondary current collector. This paper focuses on the first approach, in which a vacuum capacitor is formed between a radioactive source and a collector. As beta particles are emitted from the source, they traverse the vacuum gap and accumulate on the collector, effectively charging the capacitor. At steady state, the current delivered to an external load matches the rate of charge collection, and the resultant power is the product of this current and the developed voltage. Achieving a high electric potential is therefore essential to maximizing the energy harvested from beta particle emissions.

Previous research by Haim et al. [11–13] presents the design and testing of a novel experimental platform developed for characterizing direct charge energy harvesting using beta radiation. A Ni-63 beta source with an activity of 15 mCi (555 MBq) was used in the experiments. The device enables precise measurements of charge accumulation, electric potential, and current across variable electrode gaps, making it a versatile tool for experimental analysis. It delivers an effective current of approximately 20 pA, excluding self-absorbed particles, and has a specific power output of 100 μW per Curie. This study's simulations are intended to compare the experimental apparatus used by Haim et al. [11].

1.2. Ion-chamber dosimeter

An ionization chamber is a fundamental radiation detection device that measures the ionization of gas molecules due to incident radiation. It is widely used in radiation dosimetry, environmental monitoring, and nuclear instrumentation due to its simplicity, reliability, and ability to measure a wide range of radiation intensities [14].

The working principle of an ionization chamber is based on the ionization of gas molecules within a defined volume when exposed to ionizing radiation. The chamber typically consists of a gas-filled enclosure with two electrodes: a positively charged anode and a negatively charged cathode. When radiation passes through the gas, it ionizes the gas molecules, creating positive ions and free electrons [15]. Under the influence of the applied electric field, positive ions move toward the cathode, and electrons move toward the anode, generating a measurable electrical current. The magnitude of this current is proportional to the intensity of the radiation, allowing for precise radiation measurements [16,17].

In this study, we aimed to perform Monte Carlo simulations to investigate the response of an ion chamber to beta radiation. We conducted a literature review on the subject, and our findings are summarized as follows.

In 2014, Kim analyzed the design characteristics of cylindrical ion chambers developed by the Korea Atomic Energy Research Institute (KAERI) [18]. The research compares experimental measurements with Monte Carlo simulations performed using the EGSnrc and MCNP4C codes. This study evaluates the energy linearity of the ion chamber's response to gamma radiation, examines the angular dependence of the signal current, and assesses the impact of variations in the length of the collecting electrode on performance. They investigated gamma radiation using ion chambers with flat-type (KAERI-F) and round-type (KAERI-SR) windows. The study observed a linear increase in electric current with increasing gamma-ray energy, from 40 keV to 1 MeV. In simulations conducted with MCNP4C, the predicted currents were consistently higher than those obtained by EGSnrc, with differences of 7.2% for KAERI-F and 31.7% for KAERI-SR.

Regarding the angular dependency of the signal current, three ion chambers were tested: KAERI-F (flat-type window), KAERI-SR (short round-type window), and KAERI-LR (long round-type window). KAERI-SR exhibited the least angular dependency, making it the most stable across various angles of incidence. Studies using MCNP4C provided better predictions of angular effects due to its superior geometric modeling capabilities compared to EGSnrc.

Regarding the effect of electrode length on current efficiency, previous studies varied the electrode length from 10 mm to 20 mm in increments of 2.5 mm, with the maximum current observed at 12.5 mm. The differences observed across these variations were minimal (within 1%) and considered negligible.

In 2019, Takata investigated the effect of applied electric fields on ionization in a parallel-plate ionization chamber exposed to ^{60}Co γ-rays [19]. The study aimed to enhance theoretical understanding and align calculations with experimental data by evaluating how the signal current responds to both positive and negative voltages using EGS5 Monte Carlo simulations. It was found that, regarding the impact of

applied voltage on signal current, the signal current increases with positive voltage and decreases with negative voltage beyond the recombination region. This change was linear and consistent with previous experimental findings. The author noted a discrepancy between simulated and experimental results: the simulated signal currents showed lower rates of increase and higher rates of decrease than the experimental data, particularly at small electrode separations. The article emphasized the importance of low-energy electrons (less than 1 keV) in ionization, noting that neglecting them led to an underestimation of ionization levels. Including them in the analysis improved the correlation with experimental results, although some minor deviations persisted.

Additionally, EGS5 simulations from this article confirmed that applied electric fields influence the signal current due to the acceleration and deceleration of secondary electrons. The inclusion of low-energy electrons again enhanced the agreement with experimental data. However, minor discrepancies persisted, highlighting the need for further refinement of the model. These findings are important for optimizing ionization chamber designs and improving the accuracy of radiation measurements.

The main goal of Kahane's study was to compare Monte Carlo simulations of electron backscattering using the EGS5 code with experimental data [20]. The study focused on several key parameters, including the backscattering coefficient, energy spectra, angular distributions, and angle-dependent energy spectra.

One of the experiments [20] involved 124 keV electrons interacting with beryllium, a specific scintillator, and silicon. Their results demonstrated that EGS5 closely matched the experimental data, particularly for silicon, while the Geant4 Monte Carlo tool underperformed and required parameter tuning.

Another experiment [20] used a range of 10–30 keV on carbon, aluminum, copper, gold, and copper-gold alloys. They found good agreement at standard incidence angles ($\alpha = 0°$), but discrepancies emerged at oblique angles ($\alpha \neq 0°$), likely due to differences in the experimental setup.

Another examined angular distributions with 5–30 keV electrons on gold samples, revealed inconsistencies at high angles of incidence [20]. A final experiment [20] involved energies from 3–14 MeV on gold samples, showing that while EGS5 performed reasonably well at high energies, the simulated backscattering coefficients were consistently lower than the experimental values at MeV levels. This discrepancy is likely due to the omission of secondary electrons in the calculations.

Kahane's work [20] confirms that EGS5 is a viable Monte Carlo simulation tool for electron backscattering, demonstrating reasonable accuracy across a range of energies. While EGS5 performs well in the keV range, discrepancies arise at MeV levels, likely due to the omission of secondary processes, such as bremsstrahlung-induced electrons. It is also important to note that the article did not account for the effects of an applied electric field in its simulations, which is a significant factor.

While previous literature has explored ionization chamber performance using gamma radiation sources, alternative simulation tools, or non-parallel geometries [21,22], these studies often omit the specific parameters required for energy harvesting. To the best of our knowledge, no prior research has systematically examined the combined effects of chamber gas composition and applied electrode voltage on beta-radiation

energy harvesting. The genuine novelty of this work lies in the explicit integration of static electrostatic field tracking within the EGS5 Monte Carlo framework for a specific gas-filled harvester geometry. By directly comparing simulated spatial dose distributions with experimental ionization currents, this study establishes a validated predictive model that bridges fundamental electron-transport physics with practical device-optimization metrics for long-life beta-radiation batteries.

2. Methods

2.1. Monte Carlo simulation

Our study's novelty lies in integrating the electrostatic field within the ion chamber region into the simulation code. We compared the simulation results to previously measured data [23].

Monte Carlo techniques are instrumental in a wide range of applications, including radiation transport, nuclear reactor simulations, and medical imaging [24]. In radiation physics, for example, Monte Carlo simulations model the interactions of photons and electrons with matter, helping researchers enhance their understanding of energy deposition, radiation shielding, and dosimetry. The accuracy of these simulations improves with the number of random samples generated (iterations). However, because the method is probabilistic, the results typically include statistical error that depends on the number of simulations and the specific problem being addressed.

One widely used Monte Carlo code in this field is EGS5 (Electron Gamma Shower 5) [25]. It is particularly effective for simulating the transport of electrons and photons through complex materials and geometries. Because electrons interact probabilistically, determining their exact paths is impossible. One method for accurately computing the electron's trajectory involves using transport simulations based on the Monte Carlo technique. This code was selected for its ability to simulate complex geometries across a broad range of energies and for its established capability to implement electric fields in various contexts [26]. An extension of the EGS5 code has been developed to integrate electromagnetic and electrostatic effects into simulations, as described by Torii and Sugita [26]. This extension consists of several files and configurations that must be incorporated into the main code. Its functionality has been validated in previous simulations involving electrostatic fields of varying strengths [19, 27, 28]. Prior implementations that included field values relevant to the current study have demonstrated the extension's accuracy and reliability.

The geometry of the experimental system, previously published in Figure 1 of Haim et al. [11], was reproduced in the simulation for the comparisons. The chamber geometry used in the simulations is described as follows: It comprises a vacuum glass chamber with a diameter of 300 mm and a height of 450 mm. Inside the chamber, there is a parallel-plate capacitor consisting of a 38 mm by 10 mm by 0.25 mm nickel plate, on which the radioactive layer is placed. Additionally, there is a collector plate in the form of an aluminum disc with a diameter of 50 mm located a fixed distance of 10 mm from the source.

Several adjustments were made to simulate the system. The bell-shaped container

was replaced with a cylindrical one since the chamber is in the cylindrical portion of the bell. Given the chamber's dimensions and the gap between the chamber and the container, we concluded that the bell's rounded part does not significantly contribute to the system's functionality. For simplicity, we opted for a cylindrical container in our simulations.

We decided to position the radiation source at the origin of the coordinate system and accordingly placed the other elements based on their relative distances. For modeling the gas in the chamber, two cylindrical containers were created with a 0.01 cm difference in radius for the simulation. The inner cylinder was filled with gas, while the outer cylinder was made of glass (quartz), similar to the experimental setup. The entire system was enclosed within a vacuum sphere to define the simulation's boundaries. The geometric setup for the simulations is illustrated using the CGView utility, as shown in **Figure 1**.

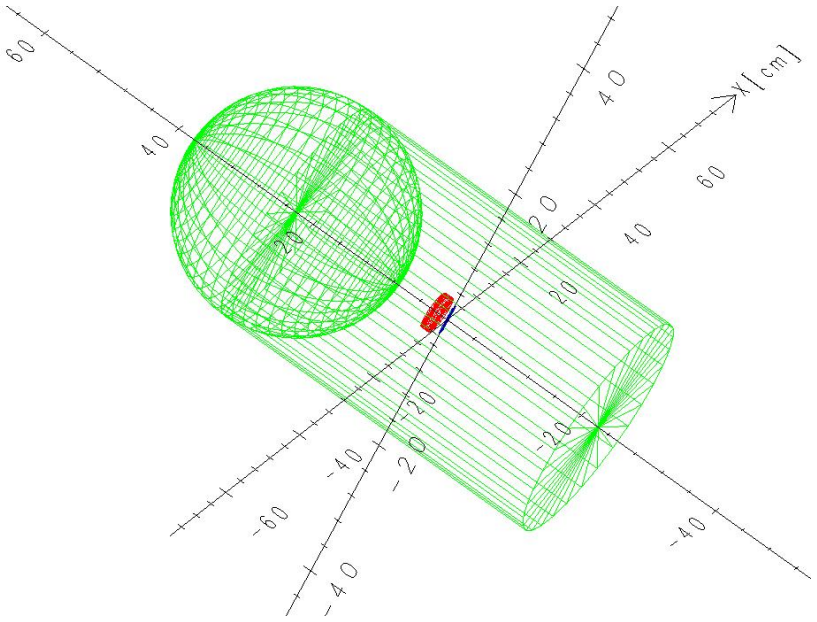

Figure 1. CGview's utility illustration of the geometrical setup.
Note: The Ion Chamber is green, the radioactive source plate is in blue, and the anode is in red.

One of the key parameters examined was the effect of the gas type within the chamber on the absorbed dose. Simulations were initially conducted for argon gas at a density of 0.001784 g/cm^3 and a pressure of 1 atm. The process was then repeated for additional gases: xenon, with a density of 0.0059 g/cm^3 at 1 atm; nitrogen, with a density of 0.001251 g/cm^3 at 1 atm; and helium, with a density of 0.0001785 g/cm^3 at 1 atm.

To accurately simulate the beta source and closely match the experimental source, we incorporated several source distributions into the code: surface distribution, emission direction, and beta-ray energy. Given that the source is thin and rectangular, we modeled its spatial distribution as a rectangular surface. We performed uniform random sampling of two variables across the surface of the source, which measures 38 mm by 10 mm. The equations implemented in the code ensure a random radiation distribution over the entire surface of the source. The angular distribution was simulated by randomly distributing the direction vector of the radiation. The half-angle between

the source and the detector is 1.4 radians (80.46 degrees). The cosine direction of the rays was uniformly distributed along 2.8 radians.

To ensure high precision in the electron trajectories under the influence of the electric field, the transport parameters were set with an electron energy cutoff (ECUT) of 0.512 MeV (representing the electron rest mass) and a photon cutoff (PCUT) of 0.01 MeV.

The spectrum of the source, Ni-63, β emission was obtained from the RADLST program, which is based on a published database [29]. A cumulative distribution function (CDF) was derived from this spectrum and fitted to a fourth-degree polynomial. This equation was then implemented in the code and incorporated into the simulation as follows:

$$\text{E\_total} = 0.512 - 0.04743\text{r} + 0.41393\text{r}^2 - 0.73648\text{r}^3 + 0.4265\text{r}^4 [\text{MeV}].$$

In this equation, r is a uniform random variable. The adjusted R-squared value for the fit is 0.99276; Fitting range: 1.65–64.25 keV. A fourth-order polynomial showed the best fit, with an R-Square of 0.99276 for our 1% precision in the MC simulation.

2.2. Electric field setup

After completing all the previous simulation setups, we incorporated the electric field into the simulations. To examine how positive and negative field values influence electron direction, we conducted a series of initial simulations using the same geometry with argon gas and a source energy of 60 keV. We ran a relatively small number of histories (30 histories), which is sufficient since generating a tracking lines file does not require many. The output files allow us to observe the particles' trajectories and geometry using the CGView program.

In this experiment, very high electric fields were applied in two scenarios: Case A featured an electric field of 10,000,000 kV/m, while Case B had a field of −100,000 kV/m. While such magnitudes are non-physical, they served to confirm the correct implementation of the electrostatic force vectors. The objective was to investigate how the polarity of the electric field (positive or negative) influences the direction of electron tracks. We define a coordinate system in which the collector anode is located at a positive distance along the Z axis relative to the source. The electric field is defined such that a positive value indicates a vector pointing from the source toward the collector. Following the relation $F = -eE$, a positive electric field exerts a force directed downward (back toward the source), causing electrons to be trapped. Conversely, a negative field points toward the source, accelerating electrons upward toward the collector, as shown in **Figure 2**.

We focused on an energy range similar to that used without the electric field, but reduced the number of simulations per run. When the electric field was integrated into the code, the simulation runtime increased significantly. It took approximately 5 days to simulate 70,000 histories with the electric field (Ar gas, Ni-63 spectrum, −1 kV), whereas simulating the same number of histories without the field took less than 1 hour. The simulations were performed on a PC featuring an Intel Core i7-4790 CPU running at 3.60 GHz with 16 GB of RAM. Each gas simulation ran for approximately 2.5 weeks.

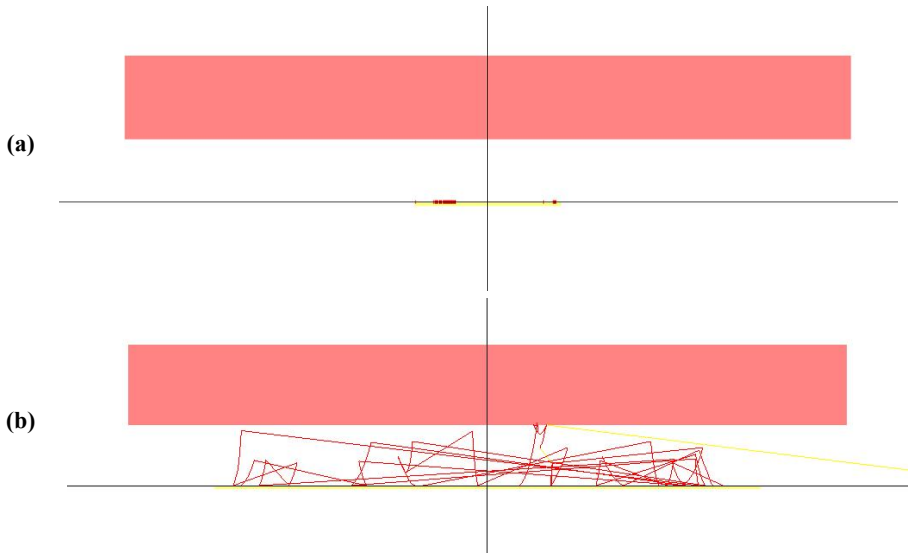

Figure 2. CGView output showing electron tracks (red lines) in the system (source in yellow, and anode in pink) under electric fields: **(a)** For positive; **(b)** For negative.

In each simulation, the absorbed dose in both the anode and the gas was tallied. This dose represents the average energy transferred to a mass m within a volume V, which is the primary quantity under investigation.

3. Results and discussion

3.1. Radiation harvester

It is necessary to obtain the energy deposited in the collector anode from radiation for radiation harvesting applications.

To establish a baseline for comparison, we initially conducted simulations without applying an electric field. A total of 12 simulations were performed. In each simulation, the electron source energy was set to a monoenergetic value between 30 and 120 keV, encompassing the commonly used electron energy range. Each simulation included 100,000 histories to obtain the desired statistical confidence level. In each simulation, the absorbed dose in the anode was tallied. The same simulation setup was conducted in an argon gas chamber with an electric field strength of 0.5 kV/m between the electrodes.

The black line in **Figure 3** represents the normalized absorbed dose results for a system without an electric field, while the red line corresponds to simulations with varying electric field strengths of 0.5 kV/m. The statistical error for each data point is approximately 0.00003%. This comparison supports the initial hypothesis that the electric field significantly influences electron transport. It also justifies proceeding with further simulations that more closely resemble the experimental setup. To calculate the variance of the results, we selected a specific energy of 100 keV and performed simulations using different random number generator seeds.

To observe the effect of electric fields on electron tracks in the chamber, we conducted brief runs consisting of 30 electrons and utilized the CGView utility to acquire the track image. Three distinct relevant cases of electron track images are shown in **Figure 4**.

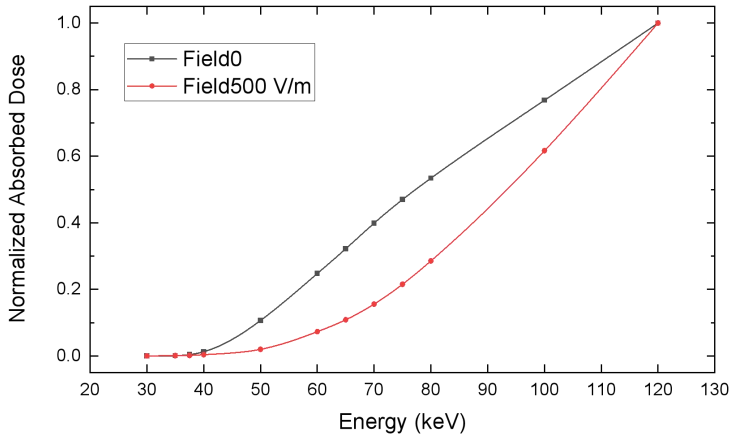

Figure 3. Simulation results of the normalized absorbed dose at 120 keV are compared between no electric field and an electric field strength of 0.5 kV/m (error bars are too small to be shown).

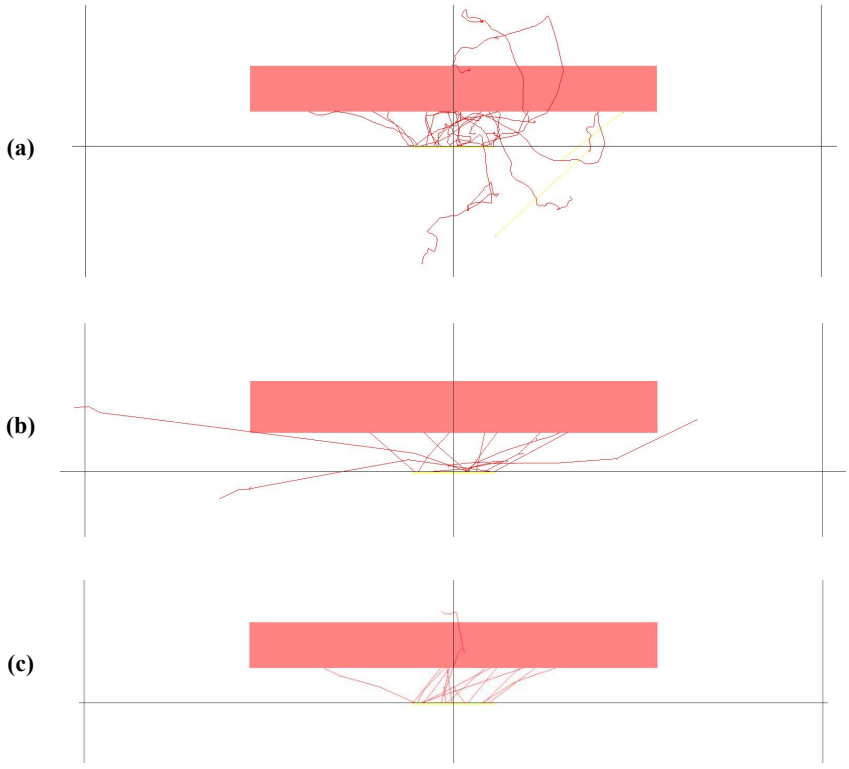

Figure 4. Electron tracks within the system under various electric field conditions: **(a)** 0 kV/m; **(b)** +10 kV/m; **(c)** −10 kV/m.

As shown in **Figure 4a**, when no electric field is applied, the electron trajectories (indicated by red lines) appear scattered and disordered because the electrons move randomly until they lose their energy and come to a stop. The yellow lines that follow the electron trajectories represent secondary photons. In contrast, when an electric field is applied, the electron trajectories become much more organized. Under a positive electric field (**Figure 4b**), some electrons are able to escape from the sides of the electrode. As anticipated, in a negative electric field (**Figure 4c**), nearly all electrons exhibit uniform motion in the same direction. These findings support our

initial hypothesis that negative electric field values are suitable for the final simulations.

We conducted a series of simulations using monoenergetic electron sources at 40 keV, 50 keV, and 90 keV. In the chamber, we introduced three different gases: argon, xenon, and nitrogen. For each gas, we performed four simulations at various electric field strengths: 0 kV/m (no electric field), −0.5 kV/m, −1 kV/m, and −15 kV/m. The absorbed doses per fluence in the collector, as a function of electron energy for each case, are presented in three graphs in **Figure 5**.

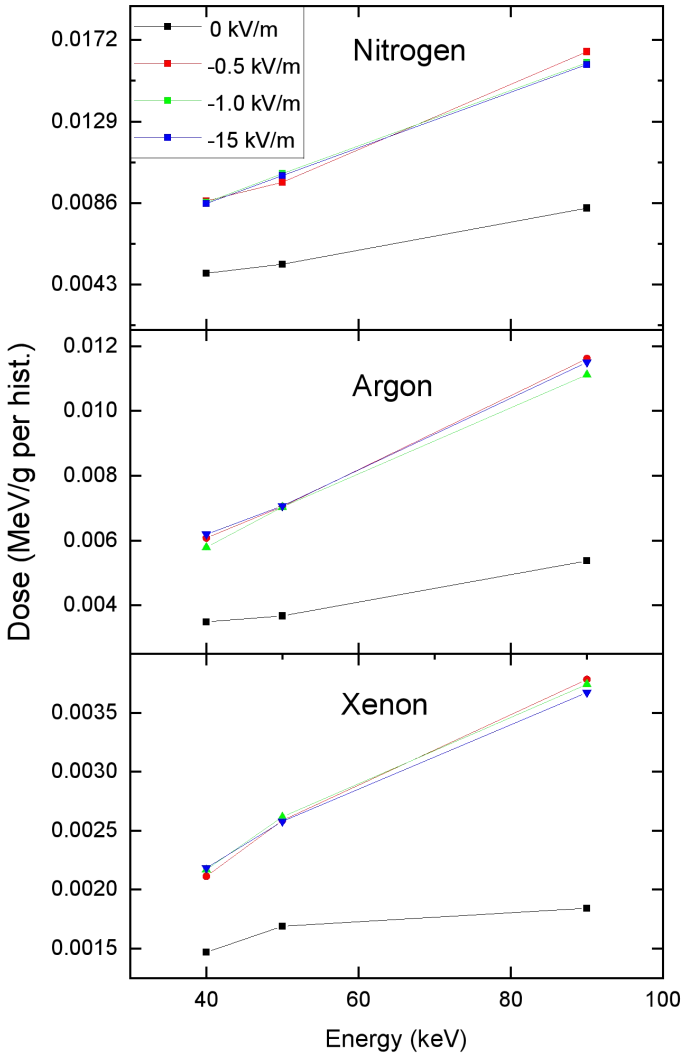

Figure 5. The deposited dose in the collector is plotted against electron energy, with electric field strengths of 0 kV/m, −0.5 kV/m, −1 kV/m, and −15 kV/m. The system included three different gases: nitrogen, argon, and xenon.

It should be noted that while Helium is utilized in experimental evaluation, monoenergetic baseline simulations were restricted to Argon, Xenon, and Nitrogen. This boundary was maintained to manage overall computational execution time and maintain manuscript conciseness, given that the preliminary monoenergetic analysis serves to establish foundational trends rather than provide a direct validation benchmark against the multi-energetic experimental setup.

In nitrogen, the induced changes in the electric field are both consistent and significant. The absorbed dose increases notably with field strength, especially at

90 keV. Compared to xenon, nitrogen offers a more efficient transfer of dose to the collector when influenced by an electric field. This increased efficiency is likely due to nitrogen's lower density, lower atomic number, and reduced interactions, which facilitate undisturbed electron transport. For argon, the absorbed dose increases almost threefold from the field-free case to the maximum field strength, particularly at higher energies. This observation indicates that the electric field becomes more effective at directing secondary electrons toward the collector as their initial energy increases. Consequently, this reduces the likelihood of energy loss due to interactions within the gas. Xenon exhibits a trend that is similar to, but slightly more moderate than, that of argon. As the field strength increases, the dose obtained in the collector also rises; however, the magnitude of this change is somewhat lower. This difference is likely due to xenon's higher atomic number and density, which enhance the probabilities of scattering and energy absorption within the gas. Nevertheless, the electric field still promotes electron drift toward the collector, as evidenced by the convergence of the high-field curves at 90 keV.

The application of an electric field enhances the collection efficiency for all three gases by decreasing the dose deposited in the gas and increasing the dose absorbed by the collector. This effect is especially noticeable at higher source energies, where electrons have greater initial kinetic energy and respond more effectively to the electric field's acceleration.

3.2. Ni-63 dose

The absorbed dose simulations were conducted using a detailed source description that included surface distribution, directional distribution, and sampling of the Ni-63 spectrum. The results of the absorbed dose simulation in the collector indicate a clear dependence on both the strength of the applied electric field and the type of gas used in the ion chamber, as shown in **Figure 6**. Generally, as the electric field strength increases, the collected dose rises slightly for nitrogen, argon, and xenon. Although this increase is modest, it is consistent, suggesting that stronger electric fields enhance electron drift toward the collector, particularly in nitrogen and argon. This effect reduces energy loss in the gas.

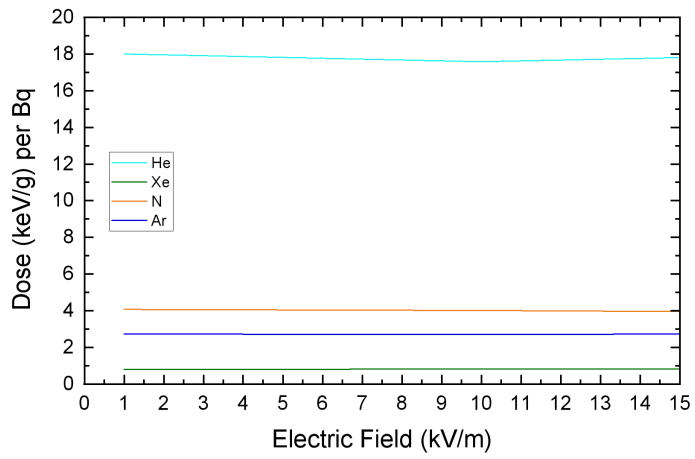

Figure 6. Absorbed dose in the collector as a function of applied electric fields in gas chambers of He, Xe, Ar, and N.

In contrast, the behavior of helium differs significantly from that of the other gases. The amount of charge collected in helium is considerably higher and remains nearly constant across all electric field strengths after an initial increase. This indicates that helium, due to its low atomic number and reduced scattering, allows for highly efficient charge collection even under relatively weak electric fields.

The simulation results shown in **Figure 6** were compared with the experimental data presented in **Figure 7**. This experimental data was collected using a consistent set of gases: helium, xenon, nitrogen, and argon, under various electric field strengths. To ensure a meaningful comparison, we concentrated on the overall trends observed in both the experimental and simulation results. Key trends included the relationship between signal magnitude and electric field strength, the relative responses of the different gases, and the saturation behavior at high field values.

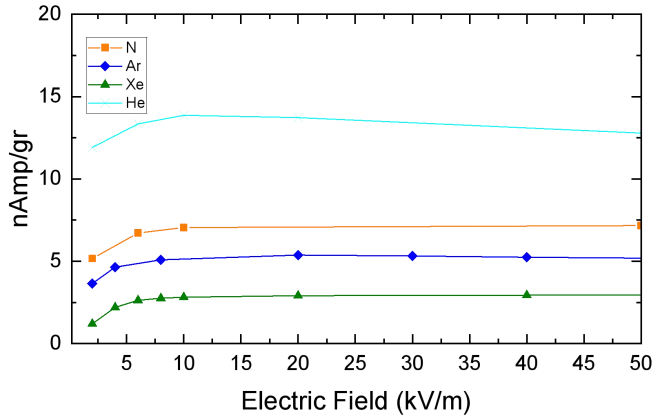

Figure 7. Experimental results showing current per gram as a function of the electric field in the collector. The measurement error is ±0.01 nA/g. Data points were obtained from Sopher et al. [23].

These insights are valuable for harvester applications that utilize continuous beta sources, such as Ni-63.

The experimental results shown in **Figure 7** indicate that the current increases as the electric field is raised to 5–10 kV/m. Beyond this point, the current tends to saturate, particularly in helium and nitrogen. This behavior suggests that at higher electric fields, most liberated electrons are efficiently collected, and further increases in field strength yield only marginal gains in current. A similar saturation behavior was observed in the simulations: the absorbed dose at the collector increased with the strength of the electric field, while the dose in the surrounding gas volume decreased, leveling off beyond approximately 5–10 kV/m. This correlation reinforces the interpretation that both the current and the absorbed dose reflect improved electron collection with stronger fields, up to a point of saturation.

The performance of different gases is consistent across both experimental and Monte Carlo simulations. Helium demonstrates the highest signals for both current and collector dose. This effectiveness is due to its low atomic number and minimal scattering, which allows for more efficient electron transport. Nitrogen and argon demonstrate intermediate responses, while xenon consistently shows the lowest values for both current and dose. This trend can be attributed to xenon's high atomic number and density, which increase the likelihood of energy loss through scattering or

absorption, ultimately reducing the number of electrons that reach the electrode [30].

It's important to note that while the absolute values of current and dose are indirectly related, the behavior of these gases in relation to the electric field shows a strong correlation. With absolute dose calibration, the simulation results can be quantitatively compared with measurements. However, a direct comparison between the simulated absorbed dose and the experimental ionization current remains primarily qualitative and trend-based. A precise quantitative conversion would require the relation $I=\frac{D \cdot m \cdot e}{W}$, where m is the gas mass, e is the elementary charge, and W is the average energy required to produce an ion pair [31]. Since the primary objective of this work is to validate the chamber's behavioral trends under varying voltages and gas environments, a qualitative trend-based comparison is fully sufficient. Since the mass and W-value remain constant for a given gas, the ionization current is directly proportional to the absorbed dose. Therefore, tracking the relative changes and saturation thresholds across different configurations provides a scientifically robust validation of the underlying transport physics without the need for absolute unit conversions.

This comparison validates the simulation approach and highlights the importance of gas properties and the electric field strength in determining electron transport and energy deposition in ion-chamber-based harvesting systems.

3.3. Ion chamber

The energy deposited by electrons in the ion chamber gas was recorded in a series of simulations using monoenergetic electron sources at 40 keV, 50 keV, and 90 keV. For each gas, we conducted four simulations at various electric field strengths: 0 kV/m (no electric field), −0.5 kV/m, −1 kV/m, and −15 kV/m. **Figure 8** illustrates the absorbed doses per fluence in the chamber as a function of electron energy for three different gases: argon, xenon, and nitrogen.

The absorbed dose in the gas decreases significantly, and as the energy increases, the difference between the curves at various field strengths becomes more pronounced. This trend indicates that the electric field becomes more effective at causing energy loss through local interactions within the gas. In nitrogen and argon, the absorbed dose in the gas decreases significantly in the presence of an electric field because the electrons are accelerated toward the electrode. In contrast, the dependence of absorbed dose on the electric field in xenon is inconsistent. This inconsistency arises from xenon's higher atomic number and density, which increases the likelihood of scattering within the gas.

It is important to note that ion-pair mobility was not considered in the ion chamber's response during these simulations. Ion mobility and recombination effects were neglected as the system operates in the saturation region, with the beta source serving as the cathode. At the electric field strengths investigated (5–10 kV/m), electron collection is highly efficient, and recombination becomes negligible.

While the ion chamber is not intended for spectral measurements, we were able to simulate the spectrum of absorbed electrons within the detector. We compared the results obtained without an electric field to those with a −1 kV/m field, using mono-energetic electron sources at 40, 49, and 90 keV. In this paper, only the argon

response spectra are presented, although we also obtained spectra for the other two gases.

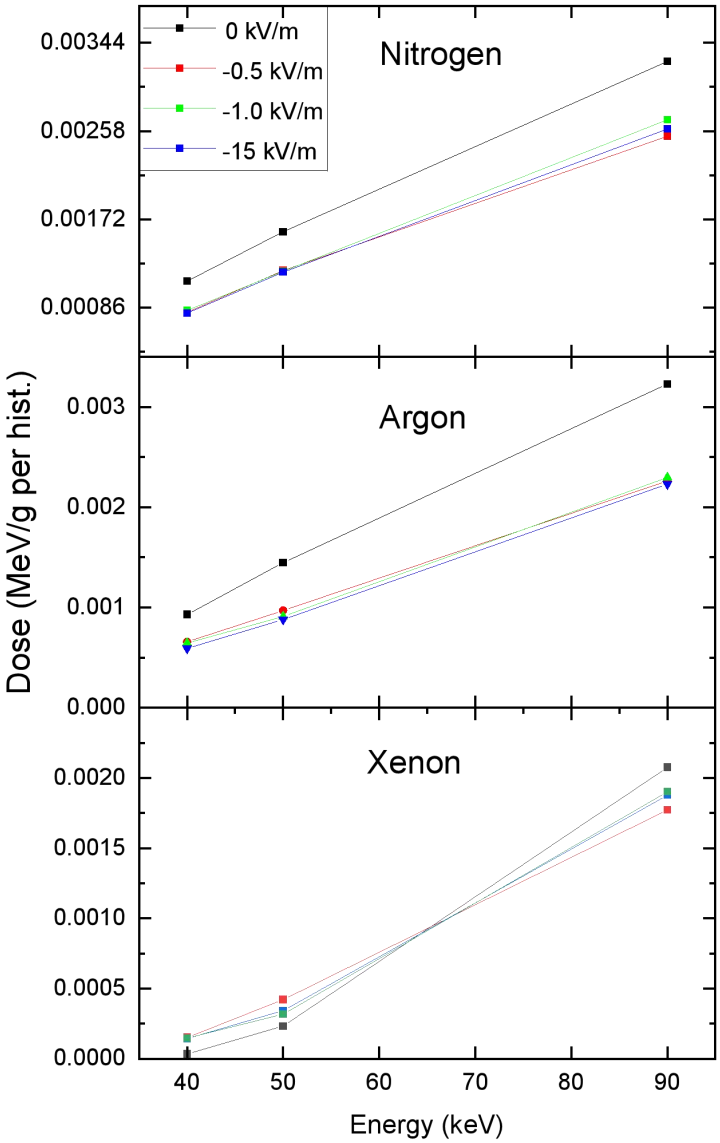

Figure 8. The absorbed dose in the gas is plotted vs. electron energy at electric field strengths of 0 kV/m, −0.5 kV/m, −1 kV/m, and −15 kV/m for three different gases: nitrogen, argon, and xenon.

The spectral results from the argon ion chamber are presented in **Figure 9**. The application of an electric field resulted in a notable increase in the proportion of low-energy electrons, as evidenced by a sharper rise in the spectral distribution at lower energies. Additionally, a significant reduction in the high-energy tail of the spectrum was observed, particularly near the energy level of the incident electron source. These findings suggest that the electric field affects electron trajectories or enhances their interactions with the gas medium, leading to increased energy loss.

When comparing the impact of the electric field across different incident energies, it is evident that lower incident energies (e.g., 40 keV) are more strongly affected by field-induced modifications, as expected. At this energy level, a substantial portion of the electron population shifted toward lower energies in all three gases. At 50 keV, the differences between the conditions with and without the electric field were

still noticeable, but they were less pronounced. At 90 keV, although the electric field continued to alter the spectral shape, the higher initial energy allowed electrons to retain a larger fraction of their energy, resulting in a reduced relative effect from the electric field. This trend was consistent across all three gases.

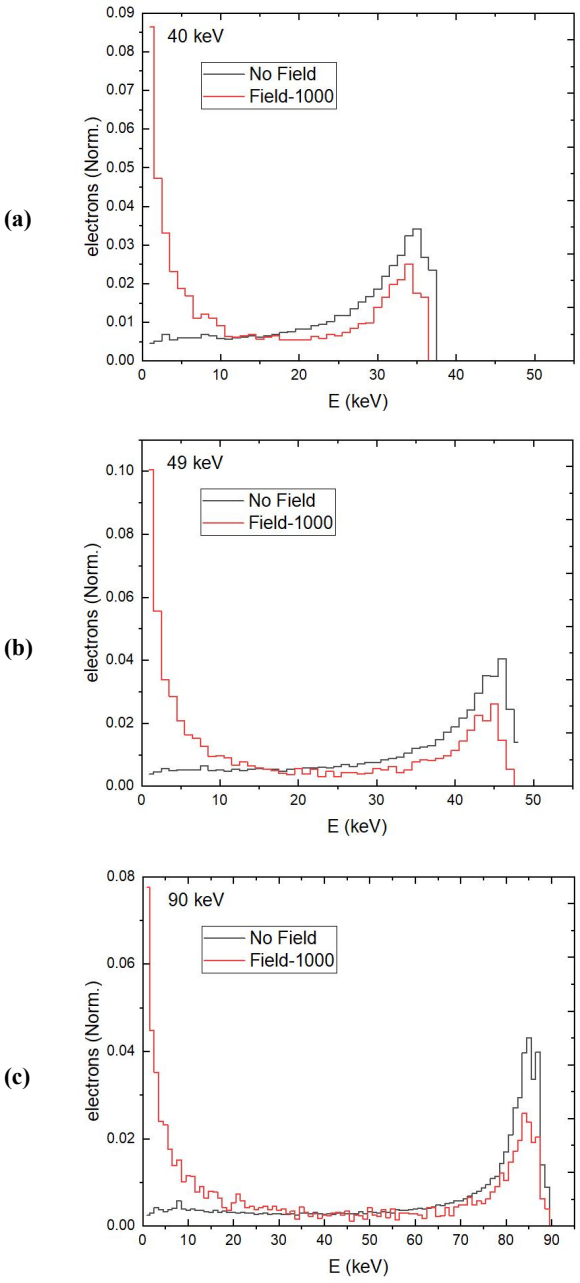

Figure 9. Energy spectrum for Argon under no electric field and −1 kV/m: **(a)** 40 keV; **(b)** 49 keV; **(c)** 90 keV.

The simulations clearly show that both the presence of an electric field and the choice of gaseous medium significantly affect the resulting electron energy spectrum. These findings highlight the importance of considering both the electric field and gas properties in applications related to electron transport and dose distribution in gaseous dosimeters.

4. Conclusion

This study developed a comprehensive simulation model to investigate the performance of an ionization chamber exposed to β-radiation (Ni-63), with particular emphasis on the effects of the applied electric field and the chamber's gas composition. A key innovation was the explicit incorporation of the electrostatic field in Monte Carlo simulations, enabling a more accurate representation of electron transport and dose deposition.

The simulation results were compared with experimental findings reported by Sopher et al. [23], which examined how gas type and electric field strength influence the ionization current. Although the studies focused on different observables—dose in simulations versus current in experiments—the underlying physics of ionization, electron transport, and energy deposition link them closely.

Both approaches revealed consistent trends:

- Saturation behavior: At electric fields of approximately 5–10 kV/m, where nearly all free electrons are collected, further increases yield only marginal improvement. Quantitatively, ramping the applied electric field from 1 to 15 kV/m results in a clear increase in the collectors' absorbed dose across all media, rising by 130.4% for xenon, 119.6% for argon, 113.8% for nitrogen, and 102.2% for helium.
- Gas-dependent performance: Helium exhibited the highest signal (both in dose and current), while xenon showed the lowest, reflecting differences in atomic structure, density, and scattering characteristics. In the multi-energetic Ni-63 spectrum, helium demonstrated superior performance, yielding an energy deposition factor nearly 18 times higher than that of xenon at the maximum electric field strength.

The agreement between simulated and experimental behaviors across gases and field strengths reinforces the validity of both methodologies. Experimental data provide practical benchmarks, while simulations offer detailed insight into underlying mechanisms, including energy-loss processes and spatial dose distributions.

Overall, these complementary studies advance our understanding of ionization chamber response under β-radiation and establish a strong foundation for optimizing such systems in applications such as long-term radiation detection, dosimetry, and β-energy conversion.

Author contributions: Conceptualization, IO; methodology, AC and ED; software, AC; validation, IO and ED; formal analysis, AC; investigation, IO and AC; resources, ED; data curation, AC; writing—original draft preparation, AC; writing—review and editing, IO; visualization, AC; supervision, IO; project administration, IO; funding acquisition, IO. All authors have read and agreed to the published version of the manuscript.

Funding: This work received no external funding.

Institutional review board statement: Not applicable.

Informed consent statement: Not applicable.

Data availability statement: Data are unavailable due to privacy.

Conflict of interest: The authors declare no conflict of interest.

AI use statement: During the preparation of this manuscript, the authors used Grammarly and ChatGPT solely for language refinement. No AI tools were used for data analysis, interpretation, or generation of scientific content. All outputs were critically reviewed and edited by the authors. The authors take full responsibility for the integrity and accuracy of the work.

References

1. Agyekum EB. Beta-voltaic nuclear batteries – review of recent developments, challenges and future research directions. Journal of Energy Storage. 2025; 122: 116701. doi: 10.1016/j.est.2025.116701
2. Yao Z, Zou F, Peng B, et al. Micronuclear batteries for nuclear waste transmutation and sustainable energy: a comprehensive review and future perspectives. Journal of Materials Chemistry A. 2026; 14(14): 7954–7978. doi: 10.1039/D5TA09148A
3. Xu M, Liu Y, Yang K, et al. Minimally invasive power sources for implantable electronics. Exploration. 2024; 4(1): 20220106. doi: 10.1002/EXP.20220106
4. Naseem MB, Kim HS, Lee J, et al. Betavoltaic Nuclear Battery: A Review of Recent Progress and Challenges as an Alternative Energy Source. The Journal of Physical Chemistry C. 2023; 127(16): 7565–7579. doi: 10.1021/acs.jpcc.3c00684
5. De Lafontaine M, Succar C, Hunter RFH, et al. Figures of merit to quantify betavoltaic device performance. Cell Reports Physical Science. 2025; 6(9): 102789. doi: 10.1016/j.xcrp.2025.102789
6. Kim HS, Rhee R, Lee J, et al. Carbon-14 Perovskite Betavoltaics Reach Record 10.79% Efficiency. Carbon Energy. 2026; 8(5): e70149. doi: 10.1002/cey2.70149
7. Daouali I, Belghachi A, Amiri B. Energy-loss process in Ni63 betavoltaic batteries. Nuclear Instruments and Methods in Physics Research Section B: Beam Interactions with Materials and Atoms. 2024; 557: 165526. doi: 10.1016/j.nimb.2024.165526
8. Liu Z, Zhou C, Lu S, et al. Energy deposition mechanisms of PbS/ZnS quantum dots in TiO_2 nanorod arrays betavoltaic cells. Applied Radiation and Isotopes. 2026; 229: 112373. doi: 10.1016/j.apradiso.2025.112373
9. Naseem MB, Lee J, In SI. Radioisotope thermoelectric generators (RTGs): a review of current challenges and future applications. Chemical Communications. 2024; 60(96): 14155–14167. doi: 10.1039/D4CC03980G
10. Takezawa H, Kigeuchi R, Umeda H, et al. Preliminary Verification of the PHITS Code Applicability to Conversion Efficiency Calculation of Direct Charge Nuclear Battery. Machines. 2024; 12(6): 395. doi: 10.3390/machines12060395
11. Haim Y, Marciano Y, deBotton G. Tunable direct beta-radiation harvester at the nanowatt scale. Sensors and Actuators A: Physical. 2018; 283: 228–234. doi: 10.1016/j.sna.2018.09.051
12. Haim Y, deBotton G. Experimental Study of the Direct-Charge Beta Radiation Method for Energy Harvesting. IEEE Transactions on Electron Devices. 2020; 67(11): 5076–5081. doi: 10.1109/TED.2020.3019360
13. Haim Y, deBotton G. Performance Analysis of the Direct-Charge β-Radiation Energy-Harvesting Method. IEEE Transactions on Electron Devices. 2021; 68(6): 2917–2925. doi: 10.1109/TED.2021.3074105
14. Knoll GF. Radiation Detection and Measurement, 4th ed. John Wiley & Sons; 2010. pp. 129–158.
15. Vialetto L, Sugawara H, Longo S. Particle Propagation and Electron Transport in Gases. Plasma. 2024; 7(1): 121–145. doi: 10.3390/plasma7010009
16. Attix FH, Introduction to Radiological Physics and Radiation Dosimetry. Wiley-VCH; 2008.
17. Muir BR, Nusrat H, Sarfehnia A, et al. Monte Carlo optimization and experimental validation of a prototype ionization chamber for accurate magnetic resonance image guided radiation therapy (MRgRT) daily output constancy measurements in solid phantoms. Medical Physics. 2022; 49(8): 5483–5490. doi: 10.1002/mp.15695
18. Kim JC, Kim JK, Kim YK, et al. Analysis of Design Characteristics of Cylindrical Ion Chamber Made by KAERI. A Comparison between EGSnrc, MCNP, and Experiment. Journal of Nuclear Science and Technology. 2004; 41(4): 299–302. Available online: https://www.tandfonline.com/doi/pdf/10.1080/00223131.2004.10875705
19. Takata N. Calculation of the effects of electric fields on ionization by electrons emitted in a parallel plate

ionization chamber irradiated with ^{60}Co γ-rays. Radiation Physics and Chemistry. 2020; 170: 108623. doi: 10.1016/j.radphyschem.2019.108623
20. Kahane S. Backscattered Electrons Spectra and Angular Distributions: Simulations with EGS5. European Journal of Engineering and Technology Research. 2018; 3(10): 95–102. doi: 10.24018/ejeng.2018.3.10.917
21. Hışıroğlu KA, Akçalı Ö, Toker O, et al. Comparative Monte Carlo study of transparent protective layers for beta radiation attenuation in betavoltaic applications. Applied Radiation and Isotopes. 2026; 229: 112358. doi: 10.1016/j.apradiso.2025.112358
22. Habib MM, Abdelgawad MH, Guirguis A, et al. Dosimetric investigation of small fields in radiotherapy measurements using Monte Carlo simulations, CC04 ionization chamber, and razor diode. Physical and Engineering Sciences in Medicine. 2025; 48(2): 813–825. doi: 10.1007/s13246-025-01546-w
23. Sopher A, Haim Y, Orion I. A Stable Current Source Based on Ionization Chamber Detector Principles. In: Proceedings of the 2023 IEEE Nuclear Science Symposium, Medical Imaging Conference and International Symposium on Room-Temperature Semiconductor Detectors (NSS MIC RTSD); 4–11 November 2023; Vancouver, BC, Canada. doi: 10.1109/NSSMICRTSD49126.2023.10337993
24. Alanazi N, Aljeraiwi R, Almutairi M, et al. A survey on recent Progress on Monte Carlo simulation methods in radiation detection. Journal of Radiation Research and Applied Sciences. 2026; 19(1): 102146. doi: 10.1016/j.jrras.2025.102146
25. Hirayama H, Namito Y, Bielajew AF, et al. The EGS5 Code System (No. SLAC-R-730, 877459). Stanford Linear Accelerator Center; 2005. doi: 10.2172/877459
26. Torii T, Sugita T. Incorporating the electromagnetic field in the EGS5 code. KEK Proceedings. 2007; 5: 43–49. Available online: https://rcwww.kek.jp/research/egs/kek/em/07-torii.pdf
27. Torii T, Sugita T, Kamogawa M, et al. Migrating source of energetic radiation generated by thunderstorm activity: Migrating source of energetic radiation. Geophysical Research Letters. 2011; 38(24). doi: 10.1029/2011GL049731
28. Torii T, Sugita T, Kamogawa M. Monte Carlo Simulation for the Source of Transient Energetic Radiation Generated by Thunderstorm Activity. Journal of Atmospheric Electricity. 2014; 34(1): 1–7. doi: 10.1541/jae.34.1
29. Eckerman KF, Westfall RJ, Ryman JC, et al. Availability of Nuclear Decay Data in Electronic Form, Including Beta Spectra Not Previously Published: Health Physics. 1994; 67(4): 338–345. doi: 10.1097/00004032-199410000-00004
30. Berger MJ. ESTAR, PSTAR, and ASTAR: Computer Programs for Calculating Stopping-Power and Range Tables for Electrons, Protons, and Helium Ions (version 1.2.3). National Institute of Standards and Technology; 2005. Available online: https://nvlpubs.nist.gov/nistpubs/Legacy/IR/nistir4999.pdf
31. International Commission on Radiation Units and Measurements. Average Energy Required to Produce an Ion Pair (ICRU Report 31). International Commission on Radiation Units and Measurements; 1979. Available online: https://inis.iaea.org/records/h6bzx-b7p74